RSC Advances

ROYAL SOCIETY OF CHEMISTRY

PAPER

View Article Online
View Journal | View Issue

Cite this: *RSC Adv.*, 2021, **11**, 15795

Conductive chitosan/polyaniline hydrogel with cell-imprinted topography as a potential substrate for neural priming of adipose derived stem cells†

Behnaz Sadat Eftekhari,[ab] Mahnaz Eskandari,*[a] Paul A. Janmey,*[b]
Ali Samadikuchaksaraei[c] and Mazaher Gholipourmalekabadi[dce]

Biophysical characteristics of engineered scaffolds such as topography and electroconductivity have shown potentially beneficial effects on stem cell morphology, proliferation, and differentiation toward neural cells. In this study, we fabricated a conductive hydrogel made from chitosan (CS) and polyaniline (PANI) with induced PC12 cell surface topography using a cell imprinting technique to provide both topographical properties and conductivity in a platform. The engineered hydrogel's potential for neural priming of rat adipose-derived stem cells (rADSCs) was determined *in vitro*. The biomechanical analysis revealed that the electrical conductivity, stiffness, and hydrophobicity of flat (F) and cell-imprinted (CI) substrates increased with increased PANI content in the CS/PANI scaffold. The conductive substrates exhibited a lower degradation rate compared to non-conductive substrates. According to data obtained from F-actin staining and AFM micrographs, both CI(CS) and CI(CS–PANI) substrates induced the morphology of rADSCs from their irregular shape (on flat substrates) into the elongated and bipolar shape of the neuronal-like PC12 cells. Immunostaining analysis revealed that both CI(CS) and CI (CS–PANI) significantly upregulated the expression of GFAP and MAP2, two neural precursor-specific genes, in rADSCs compared with flat substrates. Although the results reveal that both cell-imprinted topography and electrical conductivity affect the neural lineage differentiation, some data demonstrate that the topography effects of the cell-imprinted surface have a more critical role than electrical conductivity on neural priming of ADSCs. The current study provides new insight into the engineering of scaffolds for nerve tissue engineering.

Received 17th January 2021
Accepted 6th April 2021

DOI: 10.1039/d1ra00413a

rsc.li/rsc-advances

1. Introduction

Neurodegenerative disorders in the brain and spinal cord, traumatic injuries, and stroke influence the quality of life of 2 million people in the United States of America (USA) each year, and this number grows by an estimated 11 000 cases annually.[1,2] The regeneration of injured neurons is limited under normal conditions due to two main factors: post-damage scar formation and unguided axonal regrowth.[3] Due to the ineffectiveness of numerous strategies for the regeneration of neural defects, the damaged nerves' full recovery remains challenging.[4]

New studies suggest stem cells' potential for the treatment of catastrophic diseases such as neurodegeneration and cancer.[5–7] ADSCs have many advantages over other stem cells, such as the ease and low-cost procedure to harvest, abundance of tissues, low rates of aging and senescence[8,9] and the ability to release neurotrophic factors such as nerve growth factor (NGF), glial-derived neurotrophic factor (GDNF), brain-derived neurotrophic factor (BDNF), ciliary neurotrophic factor (CNTF), and fibroblast growth factor (FGF) to promote the survival of motor neurons *in vitro*.[10] Several reports have affirmed ADSCs' capability to differentiate toward neural lineage, boost axonal regeneration, myelination, and functional recovery, and protect oligodendrocytes *in vivo*.[11–15]

The stem cell environment (niche) controls the natural regeneration of damaged tissue by providing biochemical (*e.g.*, growth factors and other soluble factors) as well as biophysical cues (*e.g.*, shear stress, elastic modulus, geometry, and conductivity). Fundamental developments in tissue engineering

---

[a] *Department of Biomedical Engineering, Amirkabir University of Technology, 424 Hafez Ave, Tehran, 15875-4413, Iran. E-mail: eskandarim@aut.ac.ir; Tel: +98 21 6454 23 62*

[b] *Department of Physiology, Institute for Medicine and Engineering, University of Pennsylvania, 1010 Vagelos Research Laboratories, 3340 Smith Walk, Philadelphia, PA 19104-6383, USA. E-mail: janmey@mail.med.upenn.edu; Fax: +1 215 573 6815; Tel: +1 215 573 7380*

[c] *Cellular and Molecular Research Centre, Iran University of Medical Sciences, Tehran, Iran*

[d] *Department of Medical Biotechnology, Faculty of Allied Medicine, Iran University of Medical Sciences, Tehran, Iran*

[e] *Department of Tissue Engineering & Regenerative Medicine, Faculty of Advanced Technologies in Medicine, Iran University of Medical Sciences, Tehran, Iran*

† Electronic supplementary information (ESI) available. See DOI: 10.1039/d1ra00413a

have improved methods to control stem cell behaviors such as proliferation, migration, and differentiation by applying biophysical signals.[16] In particular, nerve tissue engineering scaffolds must present appropriate physical characteristics supplying the proper topography, mechanical elasticity, and electrical conductivity to accelerate axonal growth during regeneration.[17]

Conductive scaffolds that mimic the electrical conductivity of native tissue have shown the promising ability to promote stem cell plasticity and differentiation into specific lineages by altering their membrane depolarization.[18] Because of the involvement of endogenous electrical signals in neurogenesis, nerve growth, and axon guidance, biophysical studies of electrical signals are increasingly used to direct stem cell differentiation toward neuron-like cells.[19] Electrically conducting polymers such as polypyrrole, polyaniline (PANI), polythiophene, and their derivatives (mainly aniline oligomers and poly(3,4-ethylene dioxythiophene)) are bioactive biomaterials for controlled delivery of electrical signals to cells.[20] Despite these polymers' biocompatibility, their weak mechanical properties and poor processability require blending these polymers with other biomaterials.[20] Chitosan (CS), as a biocompatible, biodegradable, non-immunogenic, and antibacterial biomaterial, is frequently considered as a promising candidate for the fabrication of electroactive hydrogels.[21–26] It was reported previously that the biocompatibility of CS has a direct relationship with its degree of deacetylation (DD).[27,28] Films of chitosan with high DD between 74 and 90% have shown a mild inflammatory response after implantation.[29,30]

Most studies have also indicated that nanopatterned surfaces activate cell-surface proteins such as integrins, which are responsible for cell surface signal transduction, cluster assembly, and formation of focal adhesion complexes containing vinculin, paxillin, and focal adhesion kinase (FAK), which alter the arrangement and mechanical tension of the cytoskeleton.[31,32] Ultimately, the mechanotransduction pathway activated by mechanical tension changes the nucleus shape and the expression profile of genes involved in stem cell differentiation.[33] Despite much progress to attain precise control of stem cell behavior using engineered patterned substrates, high yield, reliable, safe, and cost-effective control of stem cell fate remains a challenge.

In 2013, Mahmoudi *et al.*, reported the cell imprinting method as a repeatable, valid, and cost-effective procedure for controlling stem cell fate.[34] In the cell imprinting method, a hierarchically patterned substrate (HPS) is obtained by molding substrates on a surface containing chemically fixed cells as a template to mimic the cell shape.[35] Furthermore, cell shape topography can act as a powerful regulator of cell behavior such as adhesion, differentiation, growth.

In most previous studies, silicone (*i.e.*, PDMS) was the shaping material due to its transparency, capacity to form nano/microstructures, and rubber-like elastic properties. The application of PDMS as a tissue engineering scaffold has several limitations, including non-biodegradability, poor electrical properties, complicated processes for improving this polymer's electrical conductivity, and undesirable mechanical properties.[36]

In the current study, an optimum amount of PANI (2.5% w/w) was incorporated into the chitosan matrix to obtain the desired conductivity while maintaining the flexibility and biocompatibility of chitosan.[37,38] The cell imprinting technique was then used to induce the PC12 cell morphology and topography directly on the surface of a conductive CS–PANI based hydrogel. The effects of cell-imprinted topography and conductivity, alone or in combination, on the CS–PANI substrate's biomechanical properties, as well as the morphology and induction of a pro-neural state in rat adipose-derived stem cells (rADSCs) is the focus of this study.

2. Materials and methods

2.1 Materials

Polyaniline emeraldine base (PANI EB, Mw average = 65 000), chitosan (%DD = 80, medium molecular weight), and 3-(4,5-dimethylthiazol-2-yl)-2,5-diphenyl tetrazolium bromide (MTT) were purchased from Sigma-Aldrich (St. Louis, MO, USA). Glutaraldehyde (50% w/w, analytical grade) and paraformaldehyde were acquired from Fluka (Chemie GmbH, Switzerland). AR grade *N*-methyl-2-pyrrolidone (NMP) (Sigma-Aldrich, St. Louis, MO, USA), acetic acid (Merck, Darmstadt, Germany), and methanol (Merck, Darmstadt, Germany) were used as received.

2.2 Fabrication of flat and cell-imprinted CS–PANI substrates

2.2.1 PC12 cell culture and differentiation. PC12 cells were seeded on plates coated with poly-D-lysine (PDL) (Sigma-Aldrich, USA) and laminin (Lam) (Sigma-Aldrich, USA) in Gibco™ 1640 Roswell Park Memorial Institute (RPMI) medium with 10% horse serum (HS), 5% fetal bovine serum (FBS) (Seromed, Germany) and 1% penicillin-streptomycin (Sigma-Aldrich, USA). After 24 hours, the medium was replaced with a serum-free medium containing 100 ng ml^{-1} nerve growth factor (NGF) (GeminiBio, USA) and maintained at 37 °C in a 95% humidified incubator with 5% CO_2.[39] The medium of cells was changed every 2 days until they reached 80% confluency. The cells were fixed with 4% paraformaldehyde (PFA) in phosphate buffered saline (PBS) (Sigma-Aldrich, USA) (pH = 7.4) for 2 h at 25 °C before treatment to preserve their shape during the printing process.

2.2.2 Preparation of flat CS and CS–PANI substrates. 1 wt% solution of CS was prepared by dissolving chitosan in 2% acetic acid with vigorous stirring. PANI was dissolved in *N*-methyl-2-pyrrolidone (NMP) to obtain a 0.5 wt% solution. To prepare the CS/PANI mixture (97.5 : 2.5 w/w), the desired amount of PANI/NMP solution was mixed with the chitosan solution. Then the mixture was stirred at room temperature for 24 h. Also, 0.8 ml glycerol was added to each mixture as a plasticizer while stirring. Flat CS (F(CS)) and flat conductive CS–PANI (F(CS–PANI)) substrates were fabricated by casting prepared CS and CS–PANI solutions on glass coated with PDL and Lam and dried in a vacuum oven at 37 °C for 24 h. Crosslinking the samples was carried out by immersing the film in a 0.0025% glutaraldehyde (0.5 mM) at room temperature. The prepared substrates were neutralized by washing them with 1 M NaOH solution. Subsequently, the excess acid and any trace of glutaraldehyde were removed by washing samples with PBS (pH = 7.2) and the substrates dried under vacuum for more than 24 h.

2.2.3 Fabrication of PC12 cell-imprinted CS and CS–PANI substrate. The prepared pure CS and CS–PANI solutions were poured on the fixed PC12 cells and incubated to dry at 37 °C for 48 h to create cell-imprinted CS substrates (CI(CS)) and cell-imprinted conductive CS–PANI substrates (CI(CS–PANI)). After peeling off the imprinted substrates, the samples' crosslinking was performed by immersing the film in a 0.0025% glutaraldehyde (0.5 mM) solution at room temperature. The flat and cell-imprinted substrates were removed from the residues of solvent and cell debris by washing them with 1 M NaOH solution after molding. Washing samples removed the excess acid and any trace of glutaraldehyde with PBS (pH = 7.2), and the substrates dried under vacuum for more than 24 h. Before cell culturing, UV light was also used for sterilization for 1 h. The total mass, temperature, and time of curing were the same for all prepared scaffolds.

2.3 Characterization of prepared substrates

2.3.1 Fourier-transform infrared spectroscopy (FTIR) spectra. A Thermo Nicolet Nexus FTIR spectrometer in the transmittance mode at 32 scans with a resolution of 4 cmK was used for recording the FTIR spectra of CS and CS–PANI samples. Spectra in the frequency range of 4000–400 cm^{-1} were measured using a deuterated tri-glycerine sulfate detector (DTGS) with a specific detectivity of 1×10^9 cm $Hz^{1/2}$ W^{-1}.

2.3.2 Imaging. The surface morphology of the topographical substrates and flat substrates was investigated by scanning electron microscopy (SEM) (Hitachi Japan; apparatus working at 10 keV accelerating voltage), atomic force microscopy (AFM; DME DS 95 Navigator 220), and optical microscopy (Nikon Optiphot 200). Before SEM imaging, all samples were coated with a thin layer of gold using a sputtering machine. AFM contact mode was performed using a rectangular cantilever (HQ:NSC18/Al BS, MikroMasch, Bulgaria) with a spring constant of 2.8 N m^{-1} and a conical tip of 8 nm radius. The sample's surface up to 90 μm^2 was scanned by a scan rate of 0.05 Hz and setpoint force 0.5 nN. The standard software of the instrument (JPKSPM Data Processing) was utilized for image analysis.

2.3.3 Electrical conductivity. The electrical conductivity of fabricated substrates was measured by applying a two-point probe method (Keithley, model 7517A). The electrical conductivity (σ) is obtained as the inverse of resistivity. The resistivity of three samples from each group of the substrate was measured by passing a constant current through the outer probes and recording the voltage *via* the inner probes. The resistivity of samples was calculated as follows:

$$\rho = \frac{\pi}{\ln 2}\left(\frac{V}{I}\right)t \quad (1)$$

where: I, V, and t indicate the applied current, voltage, and the sample thickness (200 μm), respectively.[37]

2.3.4 Mechanical test. The substrates were immersed in PBS to reach the equilibrium swelling before performing mechanical tests. The mechanical properties of all fabricated samples were determined using AFM. A Molecular Imaging Agilent Pico Plus AFM system (now known as Keysight Technologies 5500 AFM) with silicon nitride probes and 5 μm spherical (nominal value) tips (CP-PNPL-BSG, and a spring constant of 0.08 N m^{-1} was used to measure Young's modulus of samples.

2.3.5 Contact angle. The static (sessile drop) water contact angle of the prepared substrates was assessed using a contact angle apparatus (DSA20, Germany) at room temperature. A droplet of ultra-pure water was placed on the fixed sample surface, and the measurement was performed 3 s after equilibration. Then, a camera recorded the water contact angle of each surface. This measurement was repeated at three or more different locations on each sample to calculate the contact angle's average value.

2.3.6 Degradation rate. The *in vitro* degradation of substrates was followed in PBS (pH = 7.4) at 37 °C. Three samples from each group with ~40 mg weight were immersed in 10 ml of PBS and shaken by an orbital shaker (rotation speed of 60 rpm). At time points of 3, 7, 10, 14, 21, and 28 days, each of the samples was taken out and dried for 12 h after surface wiping, and its weight was recorded. To assess degradation, 20% of PBS was discarded and replaced by the fresh fluid at all-time points. This protocol was also used for a static experiment without shaking the sample. The following equation was used for the calculation of sample weight loss:

$$\text{Degradation (\%)} = (W_0 - W_d)/W_0 \times 100\% \quad (2)$$

where W_0 is the dry weight of the sample at time $t = 0$ and W_d is the dry sample weight after removal from the solution. The pH values of the solutions during scaffold immersion were also recorded.

2.4 CS–PANI substrates/rADSCs interaction

2.4.1 Isolation and culture of rat adipose-derived stem cells (rADSCs). Rat adipose-derived stem cells (rADSCs) were isolated and expanded by a procedure described in a published study.[40] In brief, subcutaneous adipose tissue samples were isolated by needle-biopsy aspiration. DMEM medium (GIBCO, Scotland) containing 10% (v/v) FBS and penicillin (100 IU ml^{-1})–streptomycin (100 μg ml^{-1}) was used for transportation to the cell culture laboratory. After washing the tissue sample with DMEM-based buffer three times, the samples were gently cut into small pieces and incubated with 0.05 mg ml^{-1} collagenase type I (Sigma, USA) for 1 h to digest the epididymal fat. The separated cells were collected from the resulting suspension after centrifugation at 200 × *g* for 5 minutes. The rADSCs were resuspended in DMEM supplemented with 10% FBS, 100 U ml^{-1} penicillin and, 100 μg ml^{-1} streptomycin in an incubator (37 °C, 5% CO_2). The culture medium was changed to remove non-adhered cells and debris.

2.4.2 Characterization of rADSCs by flow cytometry and immunocytochemistry. The rADSCs were examined by flow cytometry for identification of surface markers. The cells were identified for expression of mesenchymal markers such as CD29 and CD90 and the hematopoietic markers CD34 and CD45 (all antibodies obtained from Novus Biologicals company, US). Briefly, 1×10^6 cells in PBS were incubated with 1 μg of each antibody for 1 hour and then washed with PBS for 3 times. Ultimately, cells were treated with secondary antibodies and protected from light for 30 minutes. All cell preparations were analyzed by flow cytometry (FACSCalibur, BD), and data analysis was performed with FlowJo software (Tree Star). The rADSCs were also characterized by immunocytochemical staining as follows: the cells were fixed with 4% PFA in PBS for 15 min and permeabilized with 0.25% Triton X-100 in PBS for 10 min at RT. 3% BSA as blocking solution was added to samples for 30 min and incubated with the primary antibodies (diluted block solution) overnight at 4 °C. Fluorochrome-conjugated secondary antibodies were then added to samples for 1 h at RT and DAPI solution for another 10 min to stain the nucleus. Finally, the sample was rinsed with PBS 3 times. Fluorescence signals were detected using a Leica DMIRE2 microscope under the proper exciting wavelength.

2.4.3 Stem cell seeding on cell-imprinted substrates. The prepared substrates were placed into 6-well plates. rADSCs (3×10^3 cells per cm^2) were then cultured on the conductive cell-imprinted substrates, conductive flat substrates, and flat pure chitosan films. After 24 h, 600 μl cm^{-2} of fresh DMEM with 10% (v/v) FBS was added to each well to cover the substrates completely.

2.4.4 Cell viability. An MTT assay investigated the viability of rADSCs cells. To perform this test, a cell density of 2×10^4 cells per cm^2 were cultured on flat and cell-imprinted CS and CS–PANI substrates for 1 day, 3 days, 7 days, and 14 days in the incubator (37 °C, 5% CO$_2$). At these specified times, the cells were washed with PBS, and then the MTT solution was added into well. After incubation for 4 h, live cells created formazan crystals and were washed with PBS. A DMSO/isopropanol solution was added to dissolve the crystals. Finally, the optical density (OD) was measured using a spectrophotometer at a wavelength of 570 nm. The following formula determined the absorbance value:

$$\text{Absorbance value (OD)} = \text{average OD of the samples} - \text{average OD of the negative control}$$

The cell culture media without substrates and cells was considered as a negative control. The cells cultured on the cell culture plate's plastic surface served as a positive control (considered 100% cell viability). All data of the test were expressed as means ± standard deviation (SD) for $n = 4$. The Kolmogorov–Smirnov test was applied to investigate the normal distribution of each group of samples. Finally, a one-way ANOVA and Duncan test (GraphPad Prism 7 software) was performed to compare the data. $P < 0.05$ was considered a significant difference.

2.4.5 F-actin staining. Cell morphology and attachment on scaffolds were evaluated through F-actin staining. The ADSCs were cultured on different substrates at 5000 cells per cm^2. After 72 hours, cells were rinsed with 1× PBS, fixed with 4% PFA and permeabilized with 0.1% Triton X-100. After rinsing with PBS three times, Alexa-Fluor 647 phalloidin (Invitrogen) and DAPI staining (Sigma) were added to samples for 1 hour in the dark. Cells were observed and photographed under an inverted fluorescence microscope (Eclipse Ti-S, Nikon).

2.4.6 Neural lineage induction. ADSCs of the 4th passage were seeded on a six-well culture plate at a density of 5×10^5 cell per ml with 1 ml of neurosphere induction medium containing serum-free DMEM/F12 supplemented with 2% B27 (Thermo Fisher, USA), 20 ng ml^{-1} of basic fibroblast growth factor (bFGF) (Thermo Fisher, USA) and 20 ng ml^{-1} of epidermal growth factor (EGF) (Thermo Fisher, USA) for 3 days. The culture medium was changed with fresh DMDEM/F12 containing 5% FBS and kept in a cell culture incubator for 2 days. The neurospheres were observed by light microscopy (Olympus, Japan). The neurospheres were also fixed with 4% PFA in PBS (pH 7.4) for 20 min, permeabilized with 0.5% Triton X-100 in PBS for 10 min, and then immunostained with primary Oct4 antibody (1:300; Abcam) and secondary FITC-labeled antibody (1:400; Abcam). For determination of the potential of the substrates for neural lineage induction of ADSCs, the neurospheres were harvested by trypsin/EDTA (0.05% trypsin/0.5 mM EDTA, Sigma, USA), and the single cell suspension with 1×10^5 cell per ml density was seeded on substrates and treated with neural differentiation media containing retinoic acid (RA; 0.1 μM, Sigma), sonic hedgehog (Shh; 1 μg ml^{-1}, R&D Systems), 100 ng ml^{-1} glial-derived neurotrophic factor (GDNF, Invitrogen, Paisley, Scotland) and 200 ng ml^{-1} brain-derived neurotrophic factor (BDNF, Invitrogen, Paisley, Scotland) for five days.[41] The differentiation rate of the rADSCs toward neuron-like cells was determined by immunostaining of neuron-lineage specific markers.

2.4.6.1 Immunostaining. The cell morphology and expression of neuron cell-specific markers were investigated using optical and fluorescence microscopy (Nikon, Japan) to evaluate the neural differentiation capability of rADSCs on prepared substrates. After 8 days from neural induction, the cells seeded on substrates were rinsed with PBS and fixed with 4% PFA in PBS (pH 7.4) for 20 min. In the next step, the cells were permeabilized in a solution containing 0.5% Triton X-100 in PBS for 10 min. To block non-specific antibodies, the cells were incubated with 10% normal goat serum for 1 h at room temperature (0.05% Tween 20 and 1% (w/v) bovine serum albumin (BSA)). Detection and characterization of neuronal cells were carried out by staining the cells with antibodies against GFAP and MAP2. Antibodies to GFAP (1:100; Abcam) and MAP 2 (1:50; Millipore) were added to the cell medium for staining overnight at 4 °C. After cells were washed with PBS, the secondary antibody, including Alexa 488-conjugated goat anti-mouse and anti-rabbit antibodies, was added to cells and incubated for 1 h. Finally, the nuclei of cells were counterstained with DAPI. An Olympus BX51 fluorescence microscope was used to obtain fluorescence images.

2.5 Statistical analysis

Statistical analyses were performed using SPSS. Data are expressed as the mean – SD, and $p < 0.05$ was considered statistically significant.

3. Results and discussion

In the current study, the influences of cell-imprinted topography and conductivity, alone or in combination, of the CS–PANI substrates on the morphology and neural differentiation of rADSCs were evaluated. Fig. 1 represents the method of this study.

3.1 Characterization of CS–PANI substrates

3.1.1 Fourier-transform infrared spectroscopy (FTIR) spectra. The FTIR spectra of pure CS and CS–PANI blend substrates are shown in Fig. 2. In the pure CS spectrum, the quite broad peak at 3320 cm^{-1} can be assigned to the overlapping of OH and NH_2 stretches. The bands occurring at 2918 cm^{-1} and 2873 cm^{-1} are ascribed to the C–H stretching of the aliphatic group. The transmission peaks at 1660 cm^{-1} belong to the C=O in amide groups ($NHCOCH_3$) because of the partial deacetylation of CS. N–H bending is observed at 1554 and 1416 cm^{-1}. The transmission peak at 1386 cm^{-1} is due to the C–OH vibration of the alcohol groups in CS. Other main peaks observed in CS spectra involving 1299 cm^{-1}, 1254 cm^{-1}, and 1144 cm^{-1} are ascribed to anti-symmetric stretching of the C–O–C bridge and the C–O stretching, respectively.[42,43] After blending PANI with CS, a small shift of peaks can be seen for the PANI–CS composite with N–H stretching vibrations at 3290 cm^{-1}, C–H stretching, and vibrations at 2887/2861 cm^{-1}, respectively. A slight shift of peaks is also indicated with the amide I and II vibrations at 1646 cm^{-1} for the CS–PANI composite. Because of interactions between CS and PANI and conformational changes, small shifts occurred on the C–H bending vibration of the amide methyl group (1386 cm^{-1}) and the C–O stretching vibrations at 1161–1034 cm^{-1}. The characteristic transmission bands of PANI are also authenticated in the CS–PANI blend spectrum. The transmission peaks corresponding to the C=N stretching vibration of the quinonoid ring and the C=C stretching vibration of the benzenoid ring can be seen at 1554 and 1519 cm^{-1}, respectively.[44,45] The presence of these peaks confirms that the synthesized composite samples contained PANI.

3.1.2 Microscopic observation. The morphology of NGF-differentiated PC12 cells is shown in Fig. 3(a). The differentiation of PC12 cells into neuron-like cells leads to the outgrowth of neurites.[39] Analysis of the optical images demonstrates that the PDL/Lam coatings and NGF supported PC12 cell attachment and differentiation, respectively, as evidenced by the presence of neurite outgrowth. The color of pure PANI is dark green; the visible feature of CS–PANI blends was a uniform dark green color. Therefore, the morphology of the blend substrate is not optimal for optical microscopy. The surface morphology of flat substrates and PC12-imprinted substrates was investigated using SEM imaging. As shown by SEM images (Fig. 3(b) and (c)), the flat pure CS substrate has a homogeneous and smooth surface, and after adding PANI the smoothness of substrates is approximately preserved. Also, to evaluate the PC12 cell-imprinted pattern on pure CS and CS–PANI substrates, SEM and AFM images were obtained from the prepared substrates.

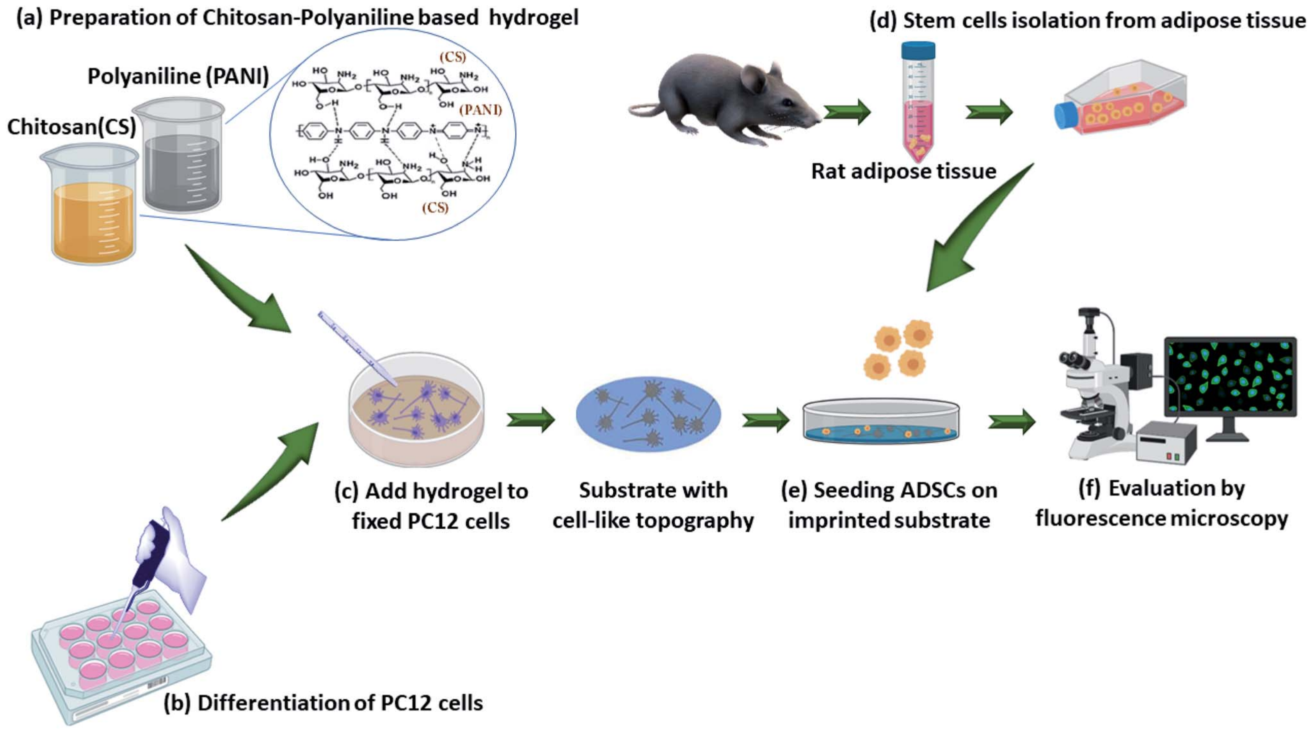

Fig. 1 Schematic representation of the experimental steps: (a) chitosan–polyaniline based hydrogel was prepared, and (b) PC12 cells were differentiated into neural cells using NGF. (c) After the fixation of these cells, PC12 morphologies were transferred to the prepared hydrogel by mold casting. In the next step, (d) stem cells were isolated from rat adipose tissue, and (e) these cells were cultured on the imprinted substrate. After 8 days, (f) the neural differentiation of rADSCs was evaluated.

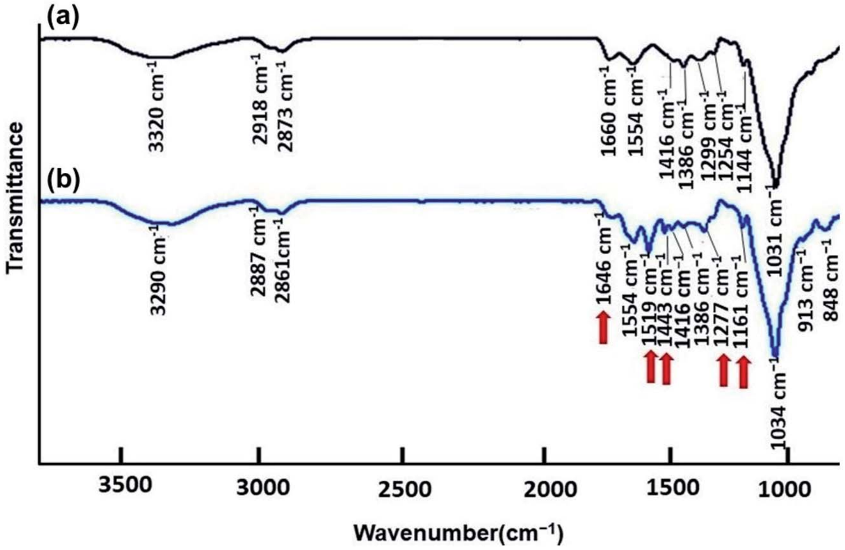

Fig. 2 FTIR spectra of (a) CS and (b) CS–PANI substrates are shown. The exhibition of peaks at 1646 cm^{-1}, 1519 cm^{-1}, 1443 cm^{-1}, 1277 cm^{-1}, and 1161 cm^{-1} peaks in the spectra of CS–PANI substrate confirm that this substrate includes PANI.

SEM micrographs of PC12-imprinted substrates are shown in Fig. 3(d)–(f). As can be seen, the replicated shapes on the substrates resemble the morphology of PC12 cells. The transferred topography on pristine CS and CS–PANI substrates mimics the large body and the network of neurites of differentiated PC12 cells. Also, the 3D AFM image (Fig. 3(g)) and a representative height profile curve for an imprinted cell (Fig. 3(h)) show the topographical features of imprinted PC12 cells on the prepared substrates. The morphology and topographical features of differentiated PC12 were investigated by Zhao *et al.*, who indicated that the PC12 cell height is between 2 to 3 μm.[46] Bonakdar and coworkers have successfully imprinted chondrocytes, tenocytes, and ADSCs morphology on PDMS. Their SEM and AFM results showed that these cells' morphology was clearly visible on the PDMS surface.[35]

3.1.3 Electrical conductivity. Fig. 4(a) illustrates all prepared samples' electrical conductivity as a function of PANI content. The substrates' conductivity is increased from 7.5×10^{-6} to 1.3×10^{-4} S m^{-1} by adding PANI to both cell-imprinted and flat CS–PANI substrates ($P \leq 0.0001$). The highly π-conjugated system of PANI strongly affected the electrical conductivity of the blend substrates and increased the conductivity of F(CS–PANI) and CI(CS–PANI) samples to 1.3×10^{-4} S m^{-1}.[44] This range of conductivity is sufficient for electrical signal conduction in *in vivo* conditions.[25]

3.1.4 Mechanical properties (stiffness measurement). According to the mechanical properties, the niche can regulate cell behavior such as attachment, migration, and differentiation, so these physical cues have been considered as an essential factor in designing the artificial microenvironment to direct the cell fate.[47] Thus, the scaffold used for nerve tissue engineering must mimic the mechanical properties of the ECM to promote the neural differentiation of stem cells.[48] The elastic moduli (Young's modulus) of substrates at different blend compositions are shown in Fig. 4(b). The pure CS substrates (flat and cell-imprinted) have lower Young's modulus compared to CS–PANI substrate (flat and cell-imprinted). The addition of PANI to flat CS substrates and cell-imprinted CS substrates increases substrate stiffness from 84.7 ± 2.7 and 77.5 ± 3.2 kPa to 108.6 ± 6.8 and 95.1 ± 2.1 kPa, respectively. This increase might be the resulted of the brittle and stiff nature of PANI (Young's modulus of PANI is 1.3 GPa),[49] as it has a tightening effect on the blends and improves the mechanical properties of the substrates. Unlike conductivity, the cell imprinting and induction of PC12 morphology decrease Young's modulus in patterned CS and CS–PANI substrates compared with those of flat CS and CS–PANI substrates, respectively. This decrease may be due to the formation of local porosity and thinning of the film after imprinting. As can be seen in Fig. 4(b), the Young's modulus of all prepared samples is between 70 and 110 kPa. According to previous studies, all of our samples' stiffness is suitable for nerve tissue engineering scaffold.[50]

3.1.5 Contact angle. The hydrophobicity of the substrate is an important characteristic that affects cell attachment. Hence, the surface wettability of the flat and cell-imprinted substrates was measured by water contact angle after treatment with sodium hydroxide (NaOH) solution (Fig. 4(c)). The contact angle increases between 40–60° by adding PANI to the substrates. Also, the cell-imprinted CS (46° ± 1.2) and CS–PANI (59° ± 2.1) substrates are slightly more hydrophobic compared to flat CS (40° ± 0.99) and CS–PANI (53.9° ± 1.8) substrates, respectively. Yang *et al.*[51] indicated that the geometrical micro- or nanostructure of the surface could increase the hydrophobicity of solid surface.[51] In earlier studies, Wenzel modified the Yang model for surfaces and stated that surface roughness enhances the wettability caused by the surface's chemistry. Young and Wenzel statements can be described with eqn (3) and (4), respectively.

$$\gamma_{\text{sv}} = \gamma_{\text{sl}} + \gamma_{\text{lv}} \cos \theta_{\text{Y}}, \tag{3}$$

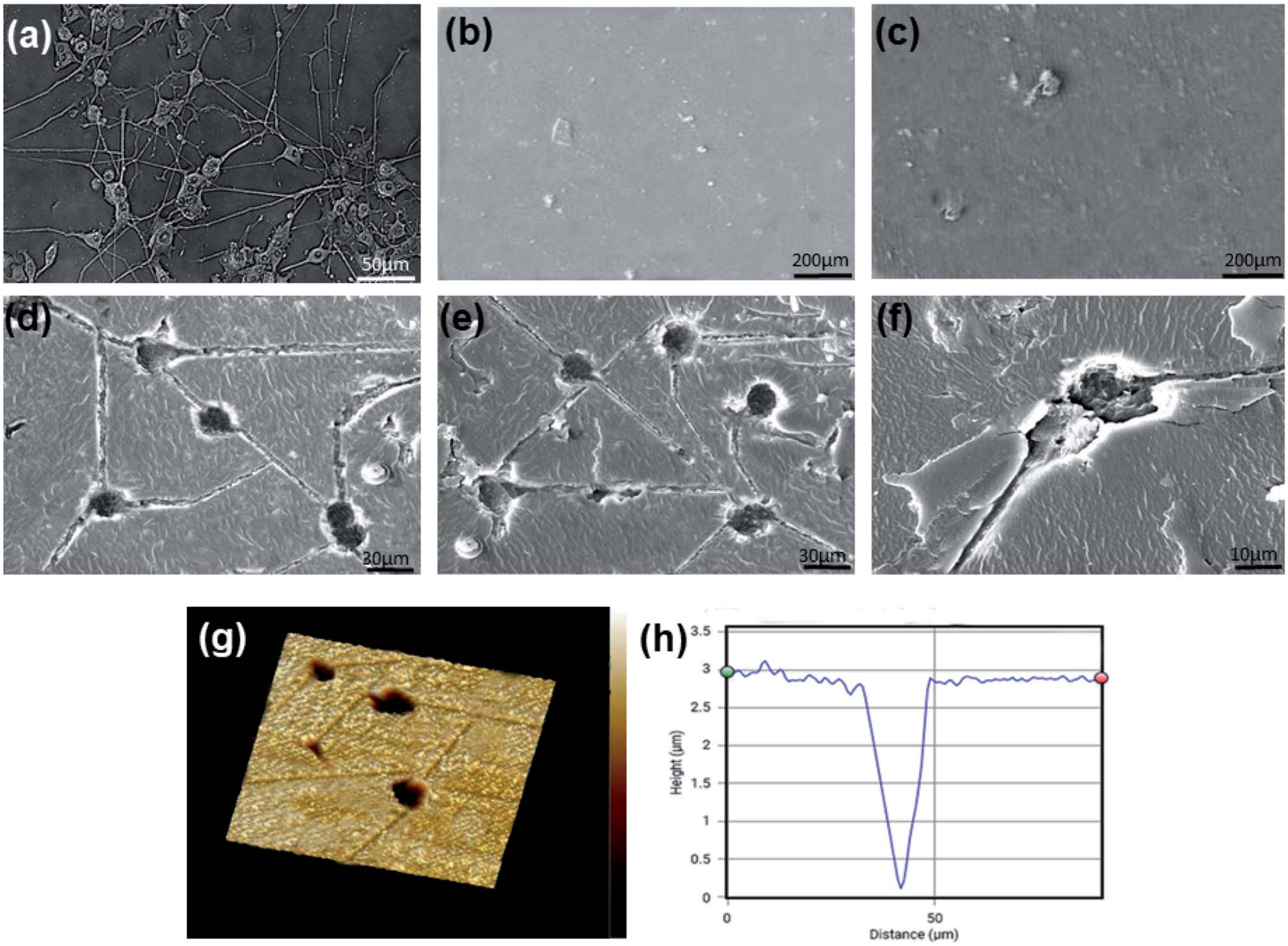

Fig. 3 (a) Optical image of differentiated PC12 cells. (b) SEM image of flat CS substrate. (c) SEM image of flat CS–PANI substrate. Topographical features of PC12 cell-imprinted substrates are shown by SEM imaging (d) PC12 cell imprinted CS substrate. (e) PC12 cell imprinted CS–PANI substrate, and (f) single PC12 cell transferred pattern on CS–PANI substrate. 3D AFM imaging (g) from a low density of PC12 cells imprinted CS–PANI substrate. (h) AFM height profile from one cell representative shape indicates the appropriate formation of the imprinted niche.

$$\cos \theta_{\mathrm{m}} = r \cos \theta_{\mathrm{Y}}, \tag{4}$$

where θ_{Y} is the Young contact angle and γ_{sv}, γ_{sl} and γ_{lv}, are liquid/gas surface tension, solid/liquid interfacial energy, and solid/gas surface energy, respectively. θ_{m} is the measured contact angle, and r is the roughness ratio. For example, the surface roughness increases the surface area, and hydrophobic surfaces with large surfaces trap higher amounts of air, leading to higher hydrophobicity. However, hydrophilic surfaces with higher roughness lead to increased polar interaction with a water droplet and decrease the water contact angle. Nevertheless, all the scaffolds fabricated in our study have moderately hydrophilic surfaces with contact angles between 40° and 70°, which are considered appropriate for the cell attachment.[52]

3.1.6 Degradation assay. Throughout *in vivo* tissue regeneration, bioengineered scaffolds should provide the support structure for cell attachment, proliferation, and differentiation.[53] The degradation of substrates in PBS solution was examined for 35 days in both static condition (ESI Fig. 1†) and after shaking the samples (Fig. 4(d)). The results show that the degradation rate of pure CS substrates is faster than other groups in both conditions. After 2 weeks CS gels still preserve approximately 53% and 60% of their initial mass after shaking and under static condition, respectively. The conductive substrates display slower degradation rates. For instance, these substrates lost approximately 34% and 30% of their mass under shaking and static conditions, respectively, over 2 weeks of incubation. This result indicates that the substrate used here possesses sufficient stability for long-term culture, which may be beneficial for inducing cell growth and differentiation. Indeed, the inherent hydrophobic nature of PANI decreases the affinity between water and the blend substrate, and the uniform incorporation of PANI in the CS substrate leads to a monotonic increase in contact angle. Therefore, the hydrophobic domain of PANI in the CS matrix decreases the hydrophilicity of the substrate and acts as a barrier against water penetration. This decrease in water penetration after addition of PANI is a plausible explanation for the decrease in degradation the rate of the CS–PANI conductive substrate compared with CS substrates.

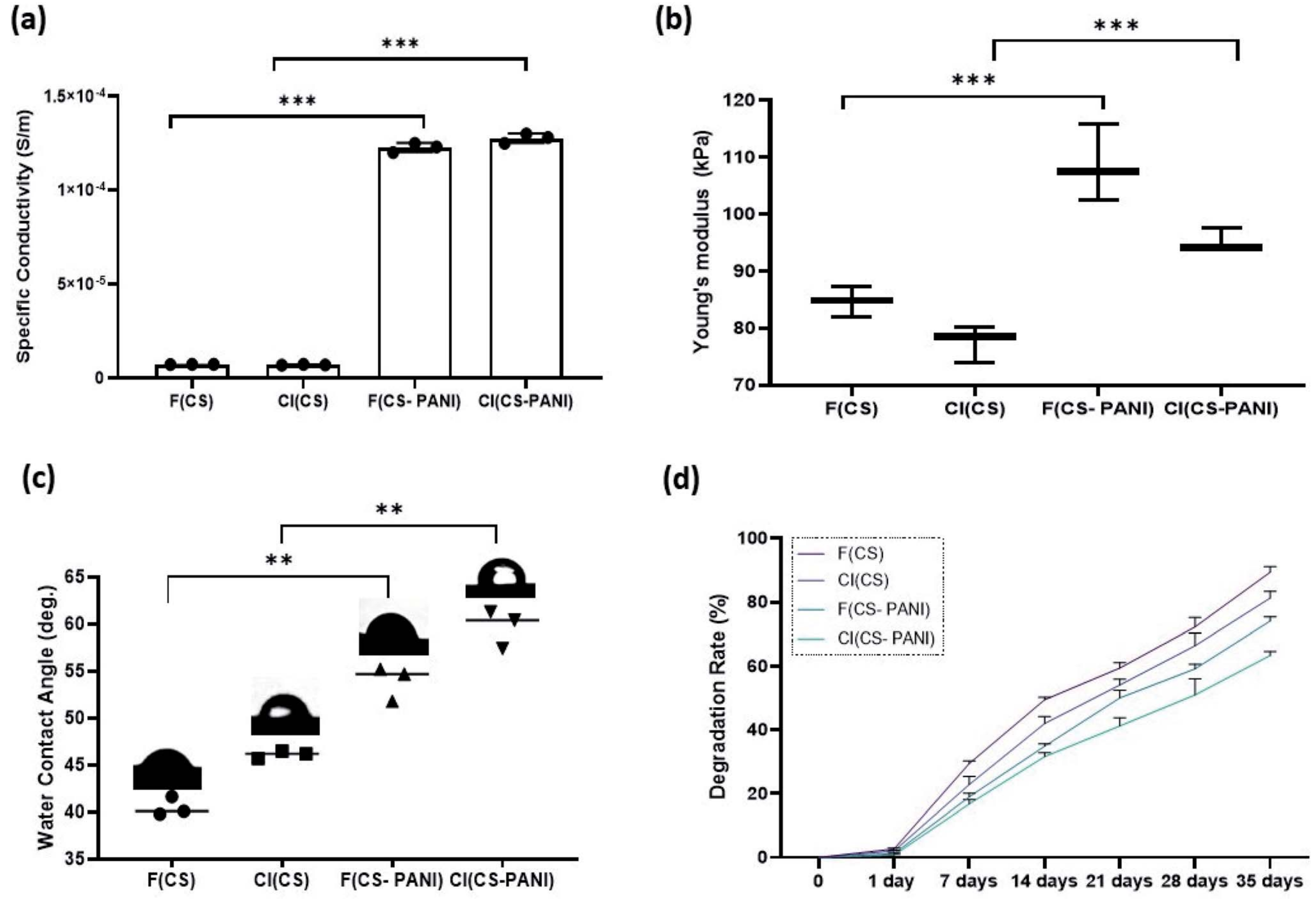

Fig. 4 (a) The electrical conductivity of the substrates was increased by adding PANI to pure CS for both flat and cell-imprinted substrates. Flat (F) and cell-imprinted (CI) substrates: F (CS), F (CS–PANI), CI (CS), CI (CS–PANI). Error bars represent the SD of measurements performed on 4 samples ($P < 0.0001$). (b) Young's modulus of fabricated flat (F) and cell-imprinted (CI) substrates: F (CS), F (CS–PANI), CI (CS), CI (CS–PANI) (***$P < 0.05$). (c) Characterization of wettability of various samples. Water contact angle measurement. (d) *In vitro* degradation of prepared substrates in PBS was examined over 35 days after shaking the samples. ****$P < 0.0001$.

3.2 Characterization of rat adipose-derived stem cells (rADSCs)

Fibroblast-like morphology and specific CD markers on the cell surface are the most important criteria for the characterization of ADSCs.[54,55] These cells are positive for mesenchymal specific markers such as CD29 and CD90 and negative for hematopoietic stems cell markers such as CD34 and CD45.[56] The morphology of ADSCs after 5 and 14 days after isolation is shown in Fig. 5(a). These cells display the adherent and typical fibroblast-like morphology under optical microscopy. Flow cytometry results demonstrate that 99.4% and 98.85% of the cell population are positive for CD90 and CD29, while only 0.122% and 0.457% of them are positive for CD34 and CD45, respectively (Fig. 5(b)). Immunostaining by CD surface markers was also performed (Fig. 5(c)–(f)). These results reveal that more than 98% of rADSCs positively express the mesenchymal stem cell markers CD29 and CD90 but do not express the hematopoietic stem cell marker CD45 and CD34 (<1%).

3.3 Cell attachment and morphology on substrates

An optimal biomimetic scaffold should support a microenvironment for cell attachment, growth, and migration.[57,58] The morphology of the rADSCs grown on the substrates was observed using F-actin staining and AFM imaging, and the results are shown in Fig. 6. F-actin staining of ADSCs cultured on flat and imprinted substrates to visualize cytoskeleton is seen in Fig. 6(a). The flattened irregular morphology of rADSCs on flat substrates and stretched bipolar shape of cells on imprinted substrates are visible in these figures. The ADSCs become slightly elongated on flat conductive CS–PANI substrates compared to flat pure CS substrates. In particular, the cell aspect ratio (which denotes the ratio of the major axis to the minor axis) (Fig. 6(b)) indicates that rADSCs cultured on cell-imprinted substrates exhibit obvious elongation and different morphology after adhering to the PC12-imprinted pattern. The measurement of rADSCs cell area on different substrates demonstrates that the cultured cells on the cell-imprinted substrate have surface areas closest to those of the PC12 cells used as control.

Fig. 6(d) and (e) display the different morphology of rADSCs grown on the cell-imprinted substrate and flat substrate as visualized by AFM. The cells' morphology on all substrates confirms the excellent cell adhesion property of prepared substrates for rADSCs. Also, it can be seen that the flattened

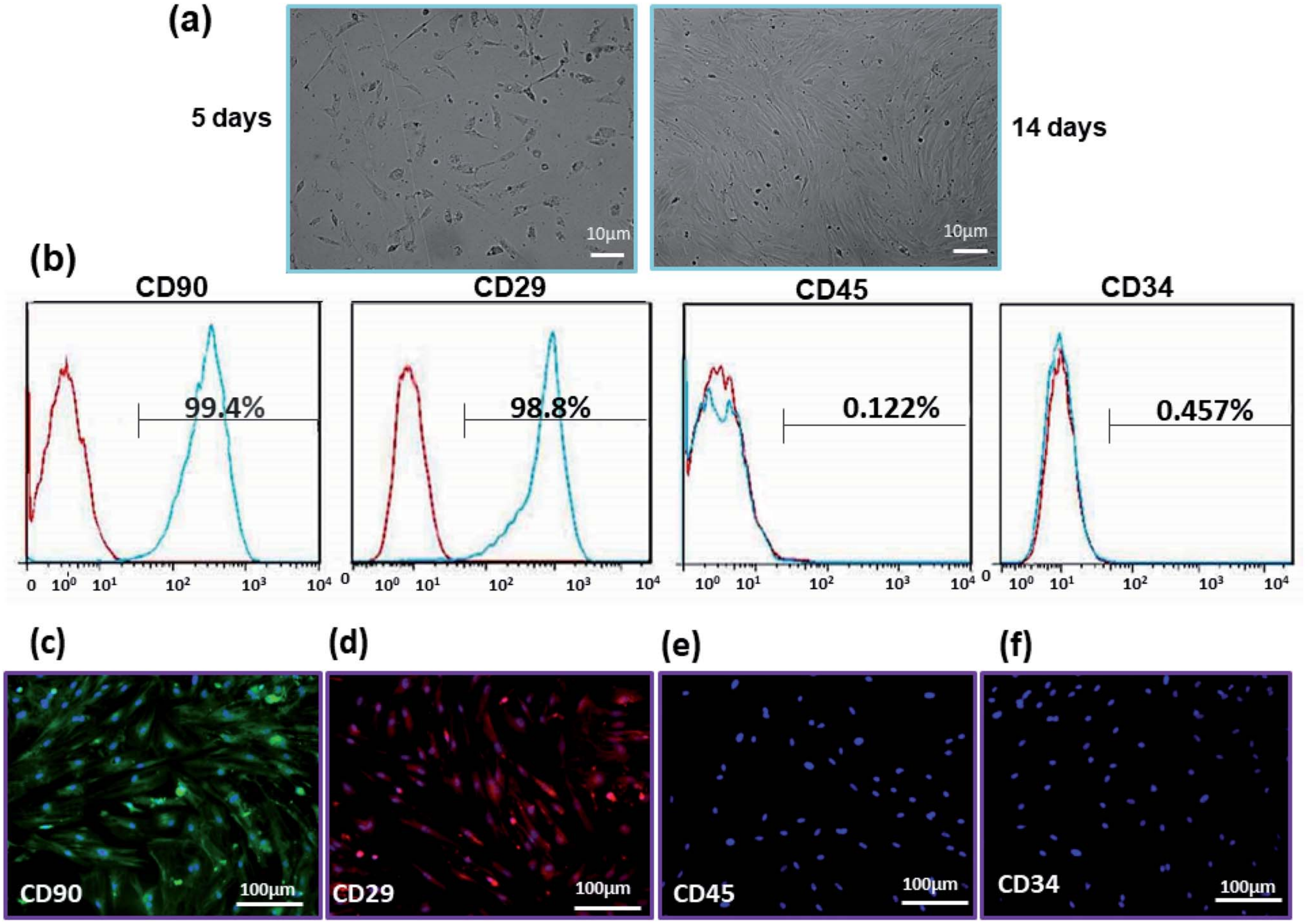

Fig. 5 (a) Morphological change in ADSCs in cell culture media at days 5 and 14 post-isolation. (b) Flow cytometry results of CD90, CD29, CD45, and CD34. More than 90% of the cell population represented phenotypic characteristics of ADSCs. Immunostaining of rADSCs expression of (c) CD90 (green), (d) CD29 (red), (e) CD45 and (f) CD34. Cell nuclei were stained with DAPI (blue). The result of staining confirmed the flow cytometry results.

irregular shape of ADSCs converts into the more elongated, bipolar shape on cell-imprinted substrates compared with flat substrates. These results support the results of F-actin staining. Height profiles of cells attached on substrates, Fig. 6(f) and (g), show the differences in the height of cultured cells on flat substrates and on cell-imprinted substrates. These findings indicate the power of the cell-imprinted topography to induce cell morphology. Although attachment and morphology of cells can be adjusted by surface chemistry, attachment forces mediated by topography might play an important role upon extended contact over time. Previous studies have shown that cells tend to adhere to rough surfaces better than smooth surfaces.[59,60]

3.4 Cell viability study (MTT assay)

The biocompatibility of pure CS substrates and CS–PANI substrates was evaluated by MTT assay to define the PANI concentration's effect on rADSCs proliferation on 1, 3, 7, 14 days after cells seeding. The determination of proliferation rate (Fig. 7) shows no significant difference between cells in the different experimental groups ($p \geq 0.05$). These results confirm the biocompatibility and supporting role of flat and cell-imprinted CS and CS–PANI substrates for the adhesion and growth of rADSCs. As PANI has concentration-dependent cytotoxicity, it is important to optimize the PANI containing conductive scaffolds in their biocompatible dose.[61] Our cell viability assay shows no sign of cytotoxicity in the CS–PANI substrates for ADSCs, indicating the optimal concentration of PANI in our constructs.

3.5 Neural lineage induction and differentiation

Several studies reported that the biophysical characteristics of scaffolds such as topographic features at the micro- and nanoscale[62] and conductivity[63] can regulate the behavior of the mammalian cells.[64,65] Micro- and nanoscale topography can direct cell fate by activating mechanotransduction pathways, rearranging the cytoskeleton and nuclear shape alignment, and ultimately altering transcription programs and protein expression.[66–68] Endogenous electric fields in tissues such as nerve, heart, and bone dictate stem cell differentiation toward a specific lineage of native tissue by altering the membrane depolarization.[69–71] Therefore, recent studies investigate the synergetic effect of these two factors on guiding stem cells' differentiation into specific cell lineage. In the current study, we

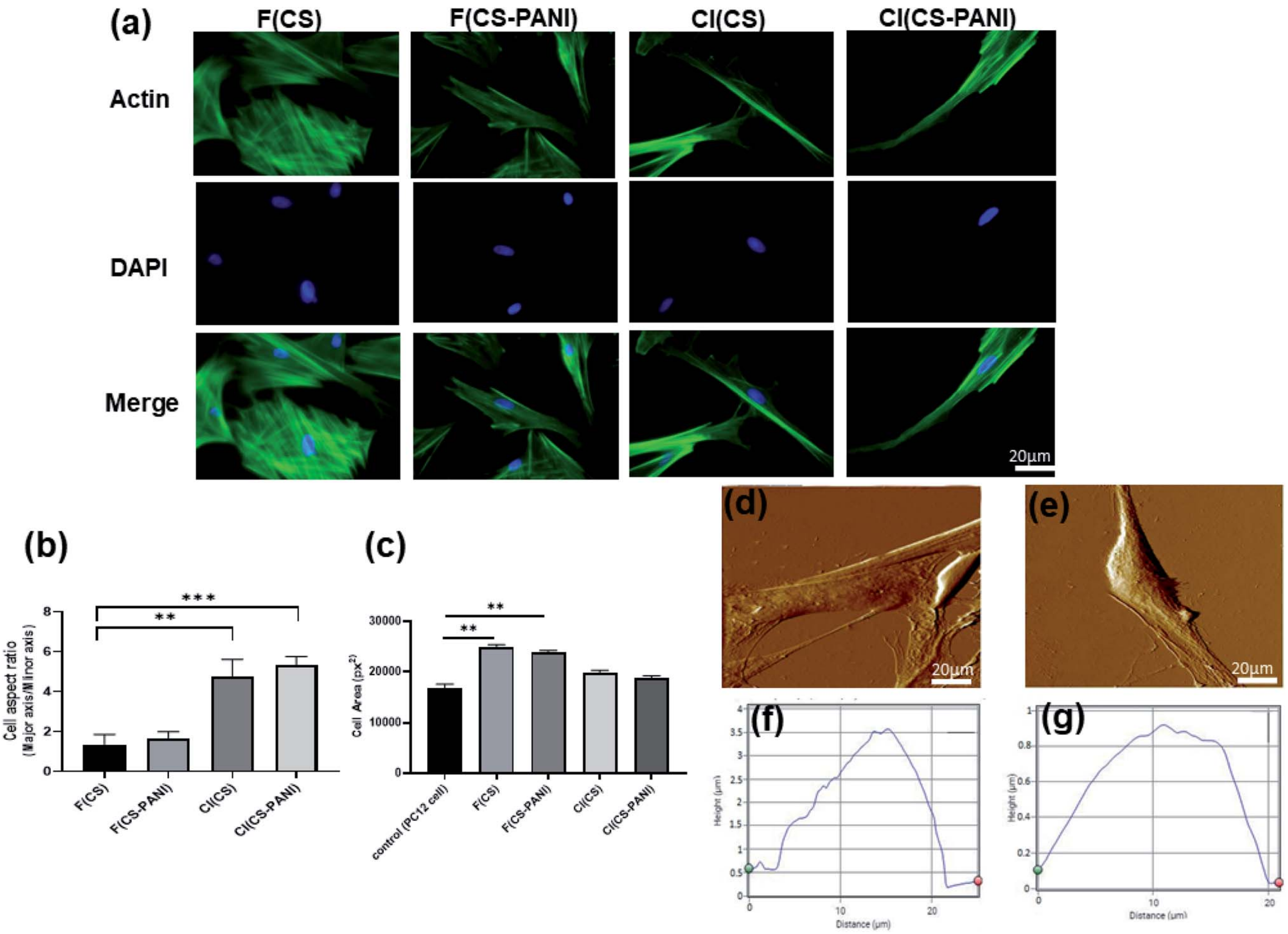

Fig. 6 Cell attachment on flat and cell-imprinted substrates. (a) F-actin in rADSCs on flat and cell-imprinted substrates was visualized by phalloidin staining 72 h of seeding. Fluorescence micrographs of rADSCs are representative images for each group. Scale bar: 20 μm. (b) Cell morphology aspect ratio of rADSCs on flat CS, flat CS–PANI, patterned pure CS, and patterned CS–PANI substrates (*$p < 0.05$). (c) The ADSCs area on different samples was compared with the PC12 cell area. AFM image of rADSCs cultured after 8 days on flat (d) and cell-imprinted (e) substrates. Scale bar: 20 μm. Height profile of cells attached on substrates. (f) Height image of ADSCs on a flat substrate. (g) Height image of ADSC on the imprinted substrate.

explored the effects of these two biophysical cues together on the guidance of neural differentiation of rADSCs.

After treatment of rADSCs with neurosphere induction media, neurosphere formation was confirmed by light microscopy (ESI Fig. 2a†) and immunostaining with Oct4 (ESI Fig. 2b†).[41] The substrates' potential for neural priming of the ADSCs was determined by immunostaining of neural precursor cell specific markers (MAP2 and GFAP) (Fig. 8). MAP2 and GFAP markers are expressed in differentiated neurons and astrocytes, respectively. The conductive samples exhibit a slight increase in the number of GFAP and MAP2 positive cells in comparison with cell-imprinted substrates with the same composition

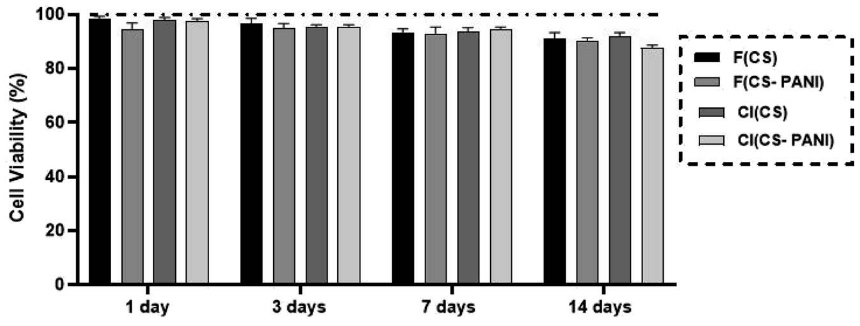

Fig. 7 MTT viability assay of cultured ADSCs on the prepared substrates. F (CS): Flat chitosan substrate, F (CS–PANI): Flat chitosan-polyaniline substrate, CI (CS): cell-imprinted chitosan substrate, CI (CS–PANI): cell-imprinted chitosan–polyaniline substrate (*$P < 0.001$).

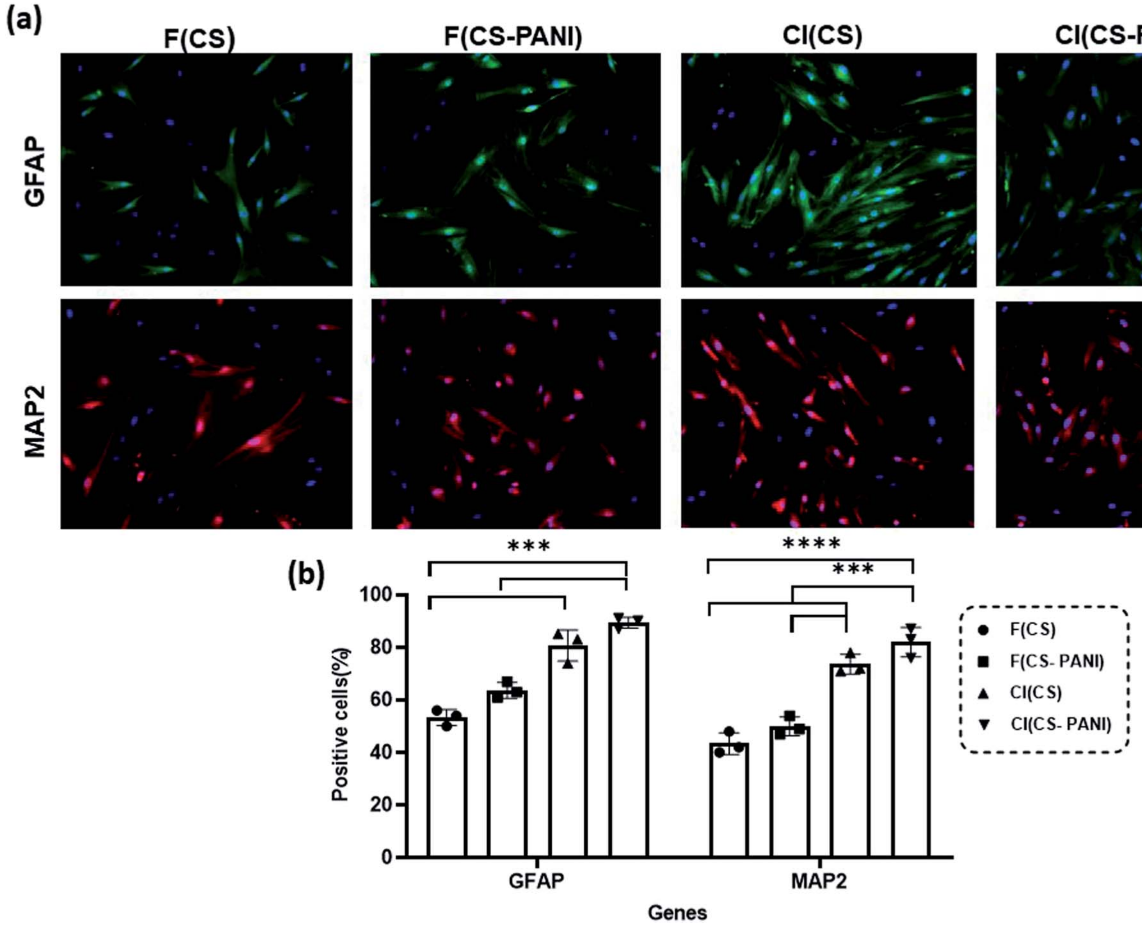

Fig. 8 (a) Immunostaining of rat adipose derived stem cell (rADSCs) expression of GFAP (green) and MAP2 (red) markers. Cell nuclei were stained with DAPI (blue). Scale bar: 100 μm. (b) Average percentage of GFAP and MAP2 expressing rADSCs. $P \leq 0.05$ was considered as level of significance. * indicates significant difference.

(F(CS–PANI) *vs.* F(CS), and CI (CS–PANI) *vs.* CI (CS)), but the increase is not statistically significant. On the other hand, all the cell-imprinted substrates show a significant increase in the GFAP and MAP2 positive cell number when compared with flat substrates with the same composition (CI (CS–PANI) *vs.* F (CS–PANI), and CI (CS) *vs.* F(CS)).

All the immunostaining data reveal the higher impact of cell-imprinting topography on the neural priming of rADSCs compared with PANI-induced conductive substrates. The results obtained from immunostaining indicate that the percentage of the cells expressing MAP2 and GFAP in the CI (CS–PANI) group (82.1 ± 5.5% MAP2 positive cells and 89.3 ± 2.1% GFAP positive cells) is higher than other experimental groups (Fig. 8(b)). The lowest percentage of GFAP (53.3 ± 3.1%) and MAP2 (43.3 ± 4.2%) positive cells is observed in the F (CS) sample when compared with other experimental groups. These results reveal the greater importance of the PC 12 cell-imprinting topography than conductivity induced with PANI on neural priming of rADSCs. Earlier studies demonstrated that cell-imprinted topography imitates the plasma membrane's surface morphology of the respective mature cell types used as templates. This topography could regulate stem cell differentiation through selective activation of the printed matured cells' genes, which lead to the autoactivation of specific complex cell signaling pathways.[34,35,72]

Also, a slight increase in the number of GFAP and MAP2 positive cells in conductive samples compared with pure CS substrates with the same surface topographical feature (F(CS–PANI) *vs.* F(CS), and CI (CS–PANI) *vs.* CI (CS)) suggests an additional role of electrical conduction in inducing of a pro-neural phenotype in ADSCs. However, we suggest that to determine better the effects of electrical conductivity induced by PANI on the cell, it is the best to apply an exogenous electrical signal to the stem cells cultured on the prepared substrate in future studies. Several studies infer that electrical stimulation is able to enhance the NGF-induced neuronal differentiation through activation of the mitogen-activated protein kinase (MEK)–extracellular signal regulated kinase (ERK1/2)–Egr1 pathway.[73–75]

Our results demonstrate that morphology and the neural priming of ADSCs are modulated by cell-imprinted topography and electrical conductivity. In our case, surface topography effects of the cell-imprinted surface have a more important role than electrical conductivity. It must be noted that although neural priming, as assessed by gene expression level (protein expression), has been observed from the induction of conductive cell-imprinted topography, the mechanisms that contribute to the changes in stem cell behaviors remain to be determined in future experiments.

4. Conclusion

The substrates produced for neurogenic differentiation effectively simulate the natural ECM of neuron cells in multiple aspects. According to our findings, the conductive cell-imprinted substrates can mimic nerve tissue's topography and conductivity, which can physically direct the stem cells' differentiation toward neuron like cells. PC12-imprinted CS–PANI substrates exhibit desirable characteristics such as appropriate mechanical properties, degradation rate, and good wettability, representing effective parameters required for neural differentiation. In conclusion, this work prepares a pioneered design of the PC12 cells morphology directly imprinted to a conductive hydrogel for controlling the morphology and neural priming of ADSCs.

Ethics approval

This article does not contain any studies with human or animal subjects performed by any of the author.

Author contributions

Behnaz Sadat Eftekhari: conceptualization, methodology, writing – original draft, data curation. Mahnaz Eskandari: supervision, formal analysis, writing – review & editing, project administration. Paul Janmey: supervision, validation, formal analysis, writing – review & editing, project administration. Ali Samadikuchaksaraei: validation and visualization. Mazaher Gholipourmalekabadi: writing – review & editing, validation and visualization.

Conflicts of interest

The authors declare that there is no conflict of interest.

Acknowledgements

The authors would like to thank the support from Amirkabir University of Technolody and the US National Science Foundation. Grants NSF DMR-1720530 and CMMI-154857.

References

1 W. A. Rocca, R. C. Petersen, D. S. Knopman, L. E. Hebert, D. A. Evans, K. S. Hall, S. Gao, F. W. Unverzagt, K. M. Langa and E. B. Larson, *Alzheimer's Dementia*, 2011, **7**, 80–93.

2 J. M. Ketchum, J. P. Cuthbert, A. Deutsch, Y. Chen, S. Charlifue, D. Chen, M. P. Dijkers, J. E. Graham, A. W. Heinemann and D. P. Lammertse, *Spinal Cord*, 2018, **56**, 126–132.

3 K. Jessen and R. Mirsky, *J. Physiol.*, 2016, **594**, 3521–3531.

4 Y. Wu, L. Wang, B. Guo, Y. Shao and P. X. Ma, *Biomaterials*, 2016, **87**, 18–31.

5 O. Lindvall and Z. Kokaia, *Nature*, 2006, **441**, 1094–1096.

6 A. Hasan, G. Deeb, R. Rahal, K. Atwi, S. Mondello, H. E. Marei, A. Gali and E. Sleiman, *Front. Neurol.*, 2017, **8**, 28.

7 N. Poovaiah, Z. Davoudi, H. Peng, B. Schlichtmann, S. Mallapragada, B. Narasimhan and Q. Wang, *Nanoscale*, 2018, **10**, 16962–16983.

8 J. Y. Chung, W. Kim, W. Im, D. Y. Yoo, J. H. Choi, I. K. Hwang, M.-H. Won, I. B. Chang, B. M. Cho and H. S. Hwang, *J. Neurol. Sci.*, 2012, **317**, 40–46.

9 S. M. Moon, W. Kim, J. Y. Chung, W. Im, D. Y. Yoo, H. Y. Jung, M.-H. Won, J. H. Choi and I. K. Hwang, *BioMed Res. Int.*, 2012, **317**(1–2), 40–46.

10 C. A. Tobias, S. S. Han, J. S. Shumsky, D. Kim, M. Tumolo, N. O. Dhoot, M. A. Wheatley, I. Fischer, A. Tessler and M. Murray, *J. Neurotrauma*, 2005, **22**, 138–156.

11 J.-L. Boulland, M. Mastrangelopoulou, A. C. Boquest, R. Jakobsen, A. Noer, J. C. Glover and P. Collas, *Stem Cells Dev.*, 2013, **22**, 1042–1052.

12 S. Gao, P. Zhao, C. Lin, Y. Sun, Y. Wang, Z. Zhou, D. Yang, X. Wang, H. Xu and F. Zhou, *Tissue Eng., Part A*, 2014, **20**, 1271–1284.

13 S. Jang, J.-S. Park and H.-S. Jeong, *Stem Cells Int.*, 2015, **2015**, 178618.

14 Y. Liqing, G. Jia, C. Jiqing, G. Ran, C. Fei, K. Jie, W. Yanyun and Z. Cheng, *NeuroReport*, 2011, **22**, 370–373.

15 S. Gao, X. Guo, S. Zhao, Y. Jin, F. Zhou, P. Yuan, L. Cao, J. Wang, Y. Qiu and C. Sun, *Cell Death Dis.*, 2019, **10**, 1–15.

16 W. F. Liu and C. S. Chen, *Mater. Today*, 2005, **8**, 28–35.

17 M. Georgiou, J. P. Golding, A. J. Loughlin, P. J. Kingham and J. B. Phillips, *Biomaterials*, 2015, **37**, 242–251.

18 W. Zhu, T. Ye, S.-J. Lee, H. Cui, S. Miao, X. Zhou, D. Shuai and L. G. Zhang, *Nanomedicine*, 2018, **14**, 2485–2494.

19 R. Zhu, Z. Sun, C. Li, S. Ramakrishna, K. Chiu and L. He, *Exp. Neurol.*, 2019, **319**, 112963.

20 B. Guo and P. X. Ma, *Biomacromolecules*, 2018, **19**, 1764–1782.

21 S. M. Ahsan, M. Thomas, K. K. Reddy, S. G. Sooraparaju, A. Asthana and I. Bhatnagar, *Int. J. Biol. Macromol.*, 2018, **110**, 97–109.

22 M. Rodríguez-Vázquez, B. Vega-Ruiz, R. Ramos-Zúñiga, D. A. Saldaña-Koppel and L. F. Quiñones-Olvera, *BioMed Res. Int.*, 2015, **2015**, 821279.

23 N. Rezaei, H. G. Hamidabadi, S. Khosravimelal, M. Zahiri, Z. A. Ahovan, M. N. Bojnordi, B. S. Eftekhari, A. Hashemi, F. Ganji and S. Darabi, *Int. J. Biol. Macromol.*, 2020, **164**, 855–862.

24 Z. A. Ahovan, S. Khosravimelal, B. S. Eftekhari, S. Mehrabi, A. Hashemi, S. Eftekhari, P. B. Milan, M. Mobaraki, A. M. Seifalian and M. Gholipourmalekabadi, *Int. J. Biol. Macromol.*, 2020, **164**, 4475–4486.

25 X. Wei, J. Liao, Z. Davoudi, H. Zheng, J. Chen, D. Li, X. Xiong, Y. Yin, X. Yu and J. Xiong, *Mar. Drugs*, 2018, **16**, 439.

26 B. Yang, J. Jiang, L. Jiang, P. Zheng, F. Wang, Y. Zhou, Z. Chen, M. Li, M. Lian and S. Tang, *Int. J. Biol. Macromol.*, 2020, **149**, 108–115.

27 R. Hu, H. Zheng, J. Cao, Z. Davoudi and Q. Wang, *J. Biomed. Nanotechnol.*, 2017, **13**, 1097–1105.

28 Q. Wang, Y. Du, L. Fan, H. Liu and X. Wang, *Wuhan Univ. J. Nat. Sci.*, 2003, **6**, 013.

29 S. Sapru, A. K. Ghosh and S. C. Kundu, *Carbohydr. Polym.*, 2017, **167**, 196–209.

30 M. Rodríguez-Vázquez, B. Vega-Ruiz, R. Ramos-Zúñiga, D. A. Saldaña-Koppel and L. F. Quiñones-Olvera, *BioMed Res. Int.*, 2015, **2015**, 821279.

31 Y. Zhang, A. Gordon, W. Qian and W. Chen, *Adv. Healthcare Mater.*, 2015, **4**, 1900–1914.

32 M. Ermis, E. Antmen and V. Hasirci, *Bioact. Mater.*, 2018, **3**, 355–369.

33 M. Ventre and P. A. Netti, *ACS Appl. Mater. Interfaces*, 2016, **8**, 14896–14908.

34 M. Mahmoudi, S. Bonakdar, M. A. Shokrgozar, H. Aghaverdi, R. Hartmann, A. Pick, G. Witte and W. J. Parak, *ACS Nano*, 2013, **7**, 8379–8384.

35 S. Bonakdar, M. Mahmoudi, L. Montazeri, M. Taghipoor, A. Bertsch, M. A. Shokrgozar, S. Sharifi, M. Majidi, O. Mashinchian and M. Hamrang Sekachaei, *ACS Appl. Mater. Interfaces*, 2016, **8**, 13777–13784.

36 A. Mata, A. J. Fleischman and S. Roy, *Biomed. Microdevices*, 2005, **7**, 281–293.

37 H. Baniasadi, A. R. SA and S. Mashayekhan, *Int. J. Biol. Macromol.*, 2015, **74**, 360–366.

38 V. Guarino, M. A. Alvarez-Perez, A. Borriello, T. Napolitano and L. Ambrosio, *Adv. Healthcare Mater.*, 2013, **2**, 218–227.

39 A. Orlowska, P. T. Perera, M. Al Kobaisi, A. Dias, H. K. D. Nguyen, S. Ghanaati, V. Baulin, R. J. Crawford and E. P. Ivanova, *Materials*, 2018, **11**, 60.

40 J. Sun, W. H. Liu, F. M. Deng, Y. H. Luo, K. Wen, H. Zhang, H. R. Liu, J. Wu, B. Y. Su and Y. L. Liu, *Exp. Ther. Med.*, 2018, **15**, 1424–1432.

41 M. Darvishi, T. Tiraihi, S. A. Mesbah-Namin, A. Delshad and T. Taheri, *Cell. Mol. Neurobiol.*, 2017, **37**, 275–289.

42 J. Nunthanid, M. Laungtana-Anan, P. Sriamornsak, S. Limmatvapirat, S. Puttipipatkhachorn, L. Y. Lim and E. Khor, *J. Controlled Release*, 2004, **99**, 15–26.

43 Z. Osman and A. K. Arof, *Electrochim. Acta*, 2003, **48**, 993–999.

44 M. R. Gizdavic-Nikolaidis, D. R. Stanisavljev, A. J. Easteal and Z. D. Zujovic, *J. Phys. Chem. C*, 2010, **114**, 18790–18796.

45 A. G. Yavuz, A. Uygun and V. R. Bhethanabotla, *Carbohydr. Polym.*, 2010, **81**, 712–719.

46 W. Zhao, W. Cui, S. Xu, L.-Z. Cheong, D. Wang and C. Shen, *Nanoscale Adv.*, 2019, **1**, 537–545.

47 D. E. Discher, P. Janmey and Y.-l. Wang, *Science*, 2005, **310**, 1139–1143.

48 S. K. Seidlits, Z. Z. Khaing, R. R. Petersen, J. D. Nickels, J. E. Vanscoy, J. B. Shear and C. E. Schmidt, *Biomaterials*, 2010, **31**, 3930–3940.

49 H. Valentová and J. Stejskal, *Synth. Met.*, 2010, **160**, 832–834.

50 R. N. Palchesko, L. Zhang, Y. Sun and A. W. Feinberg, *PLoS One*, 2012, 7(12), e51499.

51 C. Yang, U. Tartaglino and B. Persson, *Phys. Rev. Lett.*, 2006, **97**, 116103.

52 M. L. Carman, T. G. Estes, A. W. Feinberg, J. F. Schumacher, W. Wilkerson, L. H. Wilson, M. E. Callow, J. A. Callow and A. B. Brennan, *Biofouling*, 2006, **22**, 11–21.

53 F. Guilak, D. M. Cohen, B. T. Estes, J. M. Gimble, W. Liedtke and C. S. Chen, *Cell Stem Cell*, 2009, **5**, 17–26.

54 L. Jiang, J.-K. Zhu, X.-L. Liu, P. Xiang, J. Hu and W.-H. Yu, *NeuroReport*, 2008, **19**, 1015–1019.

55 M. J. Lopez and N. D. Spencer, in *Adipose-Derived Stem Cells*, Springer, 2011, pp. 37–46.

56 M. Sgodda, H. Aurich, S. Kleist, I. Aurich, S. König, M. M. Dollinger, W. E. Fleig and B. Christ, *Exp. Cell Res.*, 2007, **313**, 2875–2886.

57 S. S. Negah, Z. Khaksar, H. Aligholi, S. M. Sadeghi, S. M. M. Mousavi, H. Kazemi, A. J. Jahan-Abad and A. Gorji, *Mol. Neurobiol.*, 2017, **54**, 8050–8062.

58 M. L. Muerza-Cascante, A. Shokoohmand, K. Khosrotehrani, D. Haylock, P. D. Dalton, D. W. Hutmacher and D. Loessner, *Acta Biomater.*, 2017, **52**, 145–158.

59 F. Gentile, L. Tirinato, E. Battista, F. Causa, C. Liberale, E. M. di Fabrizio and P. Decuzzi, *Biomaterials*, 2010, **31**, 7205–7212.

60 H. Amani, H. Arzaghi, M. Bayandori, A. S. Dezfuli, H. Pazoki-Toroudi, A. Shafiee and L. Moradi, *Adv. Mater. Interfaces*, 2019, **6**, 1900572.

61 G. Kaur, R. Adhikari, P. Cass, M. Bown and P. Gunatillake, *RSC Adv.*, 2015, **5**, 37553–37567.

62 G. Abagnale, A. Sechi, M. Steger, Q. Zhou, C.-C. Kuo, G. Aydin, C. Schalla, G. Müller-Newen, M. Zenke and I. G. Costa, *Stem Cell Rep.*, 2017, **9**, 654–666.

63 K. Yang, S. J. Yu, J. S. Lee, H.-R. Lee, G.-E. Chang, J. Seo, T. Lee, E. Cheong, S. G. Im and S.-W. Cho, *Nanoscale*, 2017, **9**, 18737–18752.

64 L. Tian, M. P. Prabhakaran, J. Hu, M. Chen, F. Besenbacher and S. Ramakrishna, *Colloids Surf., B*, 2016, **145**, 420–429.

65 B. S. Eftekhari, M. Eskandari, P. A. Janmey, A. Samadikuchaksaraei and M. Gholipourmalekabadi, *Adv. Funct. Mater.*, 2020, 1907792.

66 K. Metavarayuth, P. Sitasuwan, X. Zhao, Y. Lin and Q. Wang, *ACS Biomater. Sci. Eng.*, 2016, **2**, 142–151.

67 M. J. Dalby, N. Gadegaard and R. O. Oreffo, *Nat. Mater.*, 2014, **13**, 558–569.

68 L. E. McNamara, R. J. McMurray, M. J. Biggs, F. Kantawong, R. O. Oreffo and M. J. Dalby, *J. Tissue Eng.*, 2010, **1**, 120623.

69 S. Sundelacruz, M. Levin and D. L. Kaplan, *Sci. Rep.*, 2015, **5**, 18279.

70 K. Lynch, O. Skalli and F. Sabri, *J. Funct. Biomater.*, 2018, **9**, 30.

71 G. Thrivikraman, G. Madras and B. Basu, *Biomaterials*, 2014, **35**, 6219–6235.

72 Y. Zhu, X. Liu, J. Wu, T. M. Wong, X. Feng, C. Yang, S. Wu, Y. Zheng, X. Liu and K. M. Cheung, *ACS Appl. Mater. Interfaces*, 2019, **11**, 35513–35524.

73 C. Fu, S. Pan, Y. Ma, W. Kong, Z. Qi and X. Yang, *Artif. Cells, Nanomed., Biotechnol.*, 2019, **47**, 1867–1876.

74 D. P. Bhattarai, T. I. Hwang, J. I. Kim, J. H. Lee, S. Chun, B.-S. Kim, C. H. Park and C. S. Kim, *Mater. Sci. Eng., C*, 2020, **107**, 110325.

75 E. Tomaskovic-Crook, P. Zhang, A. Ahtiainen, H. Kaisvuo, C. Y. Lee, S. Beirne, Z. Aqrawe, D. Svirskis, J. Hyttinen and G. G. Wallace, *Adv. Healthcare Mater.*, 2019, **8**, 1900425.